A 2–20-GHz Ultralow Phase Noise Signal Source Using a Microwave Oscillator Locked to a Mode-Locked Laser

Meysam Bahmanian and J. Christoph Scheytt, *Member, IEEE*

***Abstract*— In this article, we develop the theory of a special type of optoelectronic phase-locked loop (PLL). The output signal of this type of PLL is in the electrical domain and its reference oscillator, typically a mode-locked laser, operates in the optical domain. The PLL uses a balanced optical microwave phase detector (BOMPD). In order to model the optoelectronic PLL, the nonlinear characteristic function and the gain of the BOMPD are derived analytically. Using the results of the phase detector analysis, the theory of an optoelectronic PLL using such a phase detector is developed. Based on the theoretical analysis, a broadband optoelectronic frequency synthesizer with a programmable frequency range from 2 to 20 GHz is designed and implemented. Phase noise measurements show that the optoelectronic PLL frequency synthesizer achieves an integrated rms-jitter (1 kHz–100 MHz) of less than 4 fs in the frequency range from 5 to 20 GHz with a typical value of 4 fs and a minimum of 3 fs. This is the first reported wideband PLL frequency synthesizer achieving sub-10-fs integrated rms-jitter (1 kHz–100 MHz) in the frequency range from 3 to 20 GHz. A comparison with best-in-class laboratory-grade frequency synthesizers in this frequency range shows that this synthesizer achieves lower phase noise than any electronic frequency synthesizer for offset frequencies larger than 2 kHz.**

***Index Terms*— Balanced optical microwave phase detector (BOMPD), low phase noise, mode-locked laser (MLL), phase-locked loop (PLL), optoelectronic PLL.**

I. Introduction

LOW-JITTER frequency references have a wide range of applications from wireless and wireline communications, high-speed analog-to-digital converter, and digital-to-analog converter (DAC) to fundamental research facilities, such as large array telescope systems and free electron lasers (FELs) [1]. Depending on the operating principle of these frequency references, their output could be either in the electrical or in the optical domain. In the electrical domain, oven-controlled quartz oscillators and surface acoustic wave (SAW) oscillators can offer phase noise levels down to $(-120, -140)$ dBc/Hz at (1 kHz, 100 kHz) offset frequencies normalized to a 10-GHz carrier [2]–[4]. Sapphire-loaded cavity oscillators (SLCOs) exhibit better phase noise performance by approximately two orders of magnitude but with higher manufacturing cost and size [5], [6]. The so-called optoelectronic oscillators (OEOs) use a continuous-wave (CW) laser and a feedback loop in a mixed electro-optical domain and have better phase noise than quartz and SAW oscillators, but their output signal is spurious because of their long cavity [7]. The coupled optoelectronic oscillators (COEO) replace the CW laser with another optical feedback loop consisting of an optical amplifier and an optical filter. The smaller delay of the feedback path in COEO increases the intervals of the spurs in the frequency spectrum of the RF output and enhances the spectral purity [7]. Using this technique, Matsko *et al.* [8] reported a 10-GHz COEO with a phase noise of $(-125, -145)$ dBc/Hz at (1 kHz, 100 kHz) offset frequencies and Ly *et al.* [9] reported a COEO-based millimeter-wave signal generation at 90 GHz with a phase noise of $(-104, -129)$ dBc/Hz at (1 kHz, 100 kHz) offset frequencies. In the optical domain, medium-priced and compact MLLs achieve a phase noise performance better than quartz and SAW oscillators at offset frequencies above 1 kHz [10]–[12]. Further improvement of MLL phase noise (beyond or comparable with SLCOs) has been achieved using different techniques such as optical frequency division (OFD) in which one of the MLL optical comb lines is locked onto an ultrastable CW laser [6], [13]. Recently, Kalubovilage *et al.* [14] demonstrated a compact monolithic mode-locked laser (MMLL) with an exceptional open-loop phase noise performance comparable to OFD systems. Fig. 1 compares the phase noise of the state of the art for different types of reference oscillators normalized to 10-GHz carrier frequency. The phase noise scaling is based on an ideal frequency multiplier without any additive phase noise.

In addition to the phase noise performance of these oscillators, the temporal and spectral properties of their output signals should be considered according to the application. Especially, if such an oscillator is used as a reference oscillator in a PLL, a waveform with high harmonic content is desired, as it enables the designer to lock a tunable oscillator on any of these harmonics in order to maximize the output frequency range of the PLL. Quartz and SAW oscillators have usually sinusoidal output waveforms. The harmonic content of their output signals barely exceeds a few gigahertz because of their narrowband resonator and limited bandwidth of their electronic components. Therefore, higher harmonic content is usually

Manuscript received July 19, 2020; revised September 24, 2020 and December 1, 2020; accepted December 6, 2020. Date of publication January 15, 2021; date of current version March 4, 2021. This work was supported in part by Deutsche Forschungsgemeinschaft (DFG) within the projects "Optoelectronic Frequency Synthesizer with Femtosecond Diode Laser" (OFFeDi), under Grant 370491995 and "Active THz Transceiver Components" under Grant 403579441 within the Research Unit FOR 2863 "Metrology for THz Communications" (METERACOM). This article is an expanded version from the 2020 IEEE International Microwave Symposium, August 4–6, 2020. *(Corresponding author: Meysam Bahmanian.)*

The authors are with the System and Circuit Technology Group, Heinz Nixdorf Institute, Paderborn University, 33102 Paderborn, Germany (e-mail: meysam.bahmanian@uni-paderborn.de).

Color versions of one or more figures in this article are available at https://doi.org/10.1109/TMTT.2020.3047647.

Digital Object Identifier 10.1109/TMTT.2020.3047647

This work is licensed under a Creative Commons Attribution-NonCommercial-NoDerivatives 4.0 License.
For more information, see https://creativecommons.org/licenses/by-nc-nd/4.0/

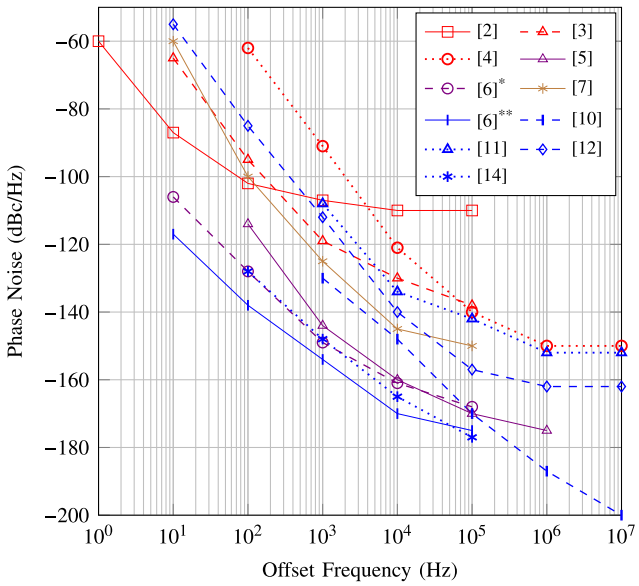

Fig. 1. Comparison of the phase noise of the state of the art, normalized to 10-GHz carrier frequency: (red) quartz and SAW oscillators, (brown) coupled OEO, (violet) SLCOs, and (blue) optical sources. [6]* and [6]** correspond to the phase noise of the SLCO and the MLL reported in [6], respectively.

generated using step recovery diodes (SRDs) or nonlinear transmission lines (NLTL) [15], [16]. The harmonic content of a COEO is limited by the bandwidth of its electronic components and the optical filter used in the feedback loop. Therefore, the spectral width of COEO is in the range of a few nanometers (less than 100 GHz) [8], [9]. In contrast to these electronic and optoelectronic reference oscillators, MLLs achieve subpicosecond pulsewidths and THz-wide optical frequency combs [10], [13], [17]. These frequency combs correspond to a harmonic rich intensity (optical cycle averaged intensity) waveform and are therefore well suited for microwave signal generation.

Many techniques have been investigated to generate a microwave signal from an MLL [18]–[22]. Among these methods, phase locking of a microwave oscillator onto an MLL using balanced optical microwave phase detector (BOMPD) is a cost-effective and relatively compact solution, as its only electro-optical components are an intensity modulator and one pair of photodetectors [22], [23]. In addition, the RF signal is mixed with the optical reference in the intensity modulator, which has a significantly higher bandwidth compared to double-balanced mixers that are typically used in high-performance fully electronic phase-locked loops. Downside of such an optoelectronic phase-locked loop (OEPLL) is the requirement for phase adjustment of its microwave signal paths and relatively sophisticated microwave setup. An alternative topology for a BOMPD proposed in [24] significantly simplifies the architecture and does not require microwave phase shifters, bandpass filters, and balanced mixers by using an electro-optical balanced intensity modulator (BIM). Fig. 2(a) shows the simplified block diagram of such an OEPLL. The BIM can be implemented using a Sagnac modulator or a Mach–Zehnder modulator (MZM), as both modulators have a similar characteristic function (see the Appendix). Using this method, Jung and Kim [25] locked a dielectric resonator oscillator (DRO) at 8 GHz onto an MLL with a residual rms-jitter of 838 as integrated from 1 Hz to 1 MHz.

The result from [25] demonstrates the potential of OEPLLs for ultralow-phase-noise frequency synthesis. However, the small bandwidth of the DRO makes the approach impractical for broadband frequency synthesis. In addition, the fiber-based Sagnac-modulator is bulky, expensive, and sensitive to mechanical vibrations. Currently, most OEPLL systems operate only at a single frequency or a very limited frequency range. Therefore, more research is needed toward microwave OEPLL frequency synthesizers with a large output frequency range and compact size. Nejadmalayeri and Kärtner [26] replaced the fiber Sagnac-modulator with a lithium-niobate ($LiNbO_3$) MZM and the DRO with a microwave instrument. This allowed to reduce the size and increase the output frequency range, but [26] did not achieve the performance of [25]. In [27], we reported the first octave-band (5–10 GHz) harmonically locked frequency synthesizer using MZM-based BOMPD and a low-cost semiconductor VCO with a sub-20-fs rms jitter performance integrated from 1 kHz to 100 MHz. In [28], we demonstrated a greatly improved version of the microwave frequency synthesizer from [27]. The frequency synthesizer can lock on any harmonic of the optical reference in the range of 2–20 GHz and achieves much lower phase noise than our previous frequency synthesizers reported in [27].

In this article, we develop a mathematical model of the OEPLL that we previously reported in [28]. Since electronic PLLs have been intensively studied using feedback systems control theory, we mainly focus on modeling the nonlinear, bias-dependent transfer characteristic of the BOMPD as a phase detector and apply it to classical PLL theory. Our derivation results match what has been derived in [29]. However, we model the effect of modulator bias voltage variation on the transfer characteristic of the BOMPD. In addition, by taking the phase of the MLL as a reference, we avoided defining unnecessary intermediate variables and lengthy discussions in [29] and provided a compact derivation. The mathematical model of the OEPLL helped us to optimize the biasing of the MZM and to adjust the PLL parameters properly.

This article is structured as follows. In Section II, we explain the operating principle of the OEPLL and the BOMPD. In Section II-A, we derive the characteristic functions of the BOMPD and develop a theory of the OEPLL based on BOMPD in Section II-B. In Section III-A, a measurement setup to characterize the BOMPD is introduced and the measured characteristic functions of the BOMPD are compared with the results derived in Section II-A. In Section III-B, an ultrawideband OEPLL with a frequency range of 2–20 GHz is demonstrated and the measured phase noise is compared with the state of the art. Section IV concludes this article.

II. Theory of Operation

A simplified block diagram of the OEPLL is shown in Fig. 2(a). The BOMPD is implemented using an MZM. It is possible to implement a BIM using a Sagnac loop instead of an MZM, as they both have similar transfer characteristics. The optical pulses of the MLL are intensity-modulated with the RF signal from the tunable oscillator, as shown in Fig. 2(b).

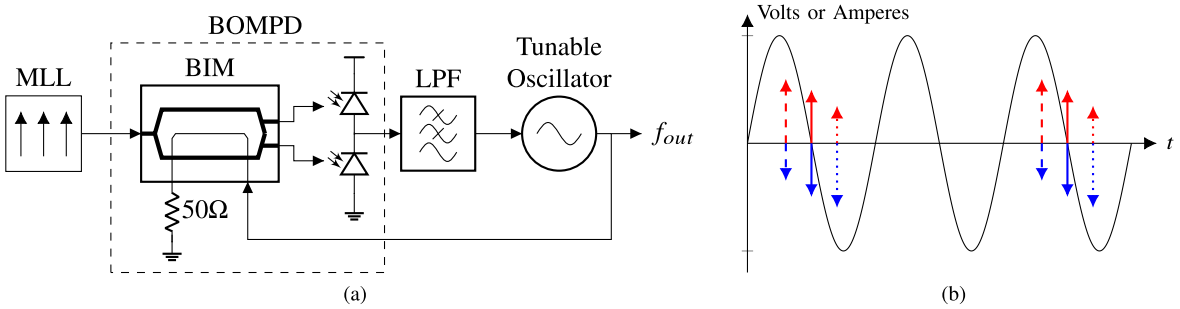

Fig. 2. (a) Simplified block diagram of the OEPLL and (b) corresponding waveforms: (black) voltage waveform at the RF port of BIM, (red) upper photodiode current, and (blue) lower photodiode current when (solid line) the phase of RF signal and the optical intensity are aligned, (dashed line) the optical intensity has a phase lead, and (dotted line) the optical intensity has a phase lag.

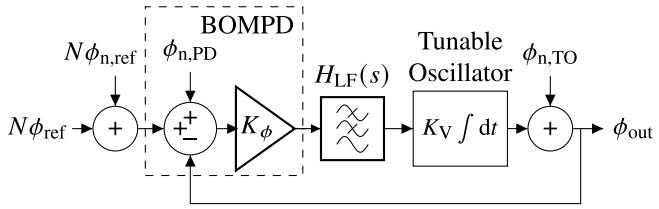

Fig. 3. Linear model of the OEPLL in the phase domain.

The modulator has two optical outputs with complementary intensities. The optical outputs of the modulator are then converted to electrical currents and subtracted using a pair of photodiodes connected in series. This current is then integrated at the loop filter and converted into an error voltage, which aligns the phase of the tunable oscillator with the phase of the envelope of the optical reference signal.

The intensities of the BIM outputs are equal when the RF signal is phase-aligned with the envelope of the optical reference, as shown in Fig. 2(b) with solid red and blue colors. Therefore, when the OEPLL is phase-locked, the current difference of the pair of photodiodes will be zero and the applied voltage to the tunable oscillator and its phase will not change. Any change in the phase difference causes an unbalance between the output intensities of the BIM as shown in Fig. 2(b) with the dashed and dotted blue and red optical pulses. These optical pulses generate a nonzero current difference in the pair of the photodiodes. This current difference can be considered as an error current, which is integrated by the loop filter and realigns the tunable oscillator phase.

Classical PLL theory models electronic PLLs as linear systems in phase domain using linear control theory and is well studied in many text books [30], [31]. The same theory can be applied to the OEPLL by replacing the electronic phase detector with the BOMPD. Fig. 3 shows the block diagram of the OEPLL in the phase domain, including the noise sources. The open-loop transfer function of the OEPLL is

$$H_{OL}(s) = K_\phi H_{LF}(s) K_V / s \tag{1}$$

where K_ϕ is the phase detector gain, $H_{LF}(s)$ is the loop filter transfer function, and K_V is the tuning sensitivity of the tunable oscillator. The phase transfer function of the output phase to the reference input phase can be written using the open-loop transfer function as

$$H_{CL}(s) = \frac{\phi_{out}}{\phi_{ref}}(s) = \frac{H_{OL}(s)}{1 + H_{OL}(s)}. \tag{2}$$

This transfer function describes the time-domain and the frequency-domain behavior of the OEPLL. The transfer function in (2) has a low-pass behavior and its 3-dB cutoff frequency represents the PLL loop bandwidth. The phase noise of the reference and the phase detector are also transferred to the output with the same transfer function in (2). The phase transfer function of the output phase to the tunable oscillator phase noise can also be written in terms of the open-loop transfer function

$$H_{TO}(s) = \frac{\phi_{out}}{\phi_{n,TO}}(s) = 1 - \frac{\phi_{out}}{\phi_{ref}}(s) = \frac{1}{1 + H_{OL}(s)} \tag{3}$$

where $\phi_{n,TO}$ is the tunable oscillator phase noise. Unlike (2), the transfer function in (3) has a high-pass behavior. Equations (2) and (3) show that on the one hand, inside the loop bandwidth, the phase noise of the reference oscillator and the phase detector dominates the output signal phase noise and, on the other hand, outside the loop bandwidth, the phase noise of the tunable oscillator dominates the output signal phase noise.

One must still keep in mind that the reference input of the BOMPD is in the optical domain and its output is an electrical current. Therefore, the main objective in analyzing the OEPLL is to determine the phase detector's nonlinear characteristic function, which describes its output amplitude versus the phase difference between its inputs. The linear phase detector gain, which is required for the analysis of the PLL/OEPLL in the phase domain, can then be found by deriving the slope of this characteristic function.

A. Deriving Characteristic Function of BOMPD

In this section, we derive the characteristic functions of the BOMPD, which is its output current as a function of the phase difference between its inputs. Assuming that the photodetectors in Fig. 2(a) are linear, we can directly use the output intensities of the MZM and exclude the photodiode responsivity from our equations. The intensities of the optical outputs of a loss-less MZM, I_y^+ and I_y^-, as a function of its optical input and the phase shift introduced by the modulation voltages can be written as (the derivation steps are given in the Appendix)

$$I_y^\pm = I_x\left[0.5 \pm 0.5\sin(\psi)\right] \tag{4}$$

where I_x is the intensity of the optical input and ψ is the total optical phase shift in the modulator arms. The phase shift ψ

is proportional to the dc and the RF modulation voltages

$$\psi = \psi_{\mathrm{RF}} + \psi_{\mathrm{dc}} = \frac{\upsilon_{\mathrm{RF}}\pi}{V_{\pi,\mathrm{RF}}} + \frac{\upsilon_{\mathrm{dc}}\pi}{V_{\pi,\mathrm{dc}}} \tag{5}$$

where ψ_{dc} is the optical phase shift introduced by the dc electrode, ψ_{RF} is the optical phase shift introduced by the RF electrode, $V_{\pi,\mathrm{dc}}$ is the π-voltage of the dc electrode, $V_{\pi,\mathrm{RF}}$ is the π-voltage of RF electrode, υ_{dc} is the bias voltage at the dc electrode, and υ_{RF} is the RF modulation voltage. The output differential intensity ΔI_y that corresponds to the output current of the photodetectors pair in Fig. 2(a) can be defined as

$$\Delta I_y := I_y^+ - I_y^- = I_x \sin(\psi). \tag{6}$$

We call $\psi_{\mathrm{dc}} = 0$ as the odd symmetry point and $\psi_{\mathrm{dc}} = \pm\pi/2$ as the even symmetry points since $\Delta I_y(\upsilon_{\mathrm{RF}})$ has odd and even symmetry versus υ_{RF} around these points, respectively. The MLL output is periodic and its output intensity can be formulated as

$$I_x(t) = I_{x,\mathrm{avg}} T_{\mathrm{ref}} \sum_{m=-\infty}^{+\infty} P\left(t - \frac{m}{f_{\mathrm{ref}}}\right) \tag{7}$$

where $I_{x,\mathrm{avg}}$ is the average optical intensity of the MLL output, T_{ref} is the period of $I_x(t)$, f_{ref} is the frequency of $I_x(t)$, and $P(t)$ is the energy-normalized pulse shape such that $\int_0^{T_{\mathrm{ref}}} P(t)dt = 1$. The optical pulses of the low-noise MLLs have typically subpicoseconds widths. Such low pulsewidths correspond to bandwidths of at least hundreds of gigahertz that are much more than the bandwidth of many RF systems, such as frequency synthesizers. Therefore, it is a good approximation to consider the intensity of MLL pulses as Dirac delta pulses, $P(t) = \delta(t)$. This assumption significantly simplifies the Fourier series expansion of the intensity waveform as

$$\begin{aligned} I_x(t) &= I_{x,\mathrm{avg}} T_{\mathrm{ref}} \sum_{m=-\infty}^{+\infty} \delta\left(t - \frac{m}{f_{\mathrm{ref}}}\right) \\ &= I_{x,\mathrm{avg}}\left[1 + 2\sum_{k=1}^{+\infty} \cos(k\omega_{\mathrm{ref}} t)\right]. \end{aligned} \tag{8}$$

We assume single-tone modulation of the RF electrode with an angular frequency of ω_{RF}, an amplitude of V_{RF}, and an offset phase of ϕ

$$\upsilon_{\mathrm{RF}} = V_{\mathrm{RF}} \sin(\omega_{\mathrm{RF}} t + \phi). \tag{9}$$

Combining (6) and (9), one can see that in the low V_{RF} regime ($V_{\mathrm{RF}} \ll V_{\pi,\mathrm{RF}}$) and zero dc phase shift ($\psi_{\mathrm{dc}} = 0$), the balanced MZM operates as a balanced electro-optical mixer and multiplies the intensity of the optical signal by the RF modulation amplitude. In this regime, the differential output intensity will be

$$\begin{aligned} \Delta I_y &= I_x \sin(\psi) \approx I_x \psi \\ &= \alpha I_{x,\mathrm{avg}} \sin(\omega_{\mathrm{RF}} t + \phi)\left[1 + 2\sum_{k=1}^{+\infty} \cos(k\omega_{\mathrm{ref}} t)\right] \end{aligned} \tag{10}$$

where

$$\alpha = V_{\mathrm{RF}}\pi / V_{\pi,\mathrm{RF}}. \tag{11}$$

The necessary condition for harmonic locking can be found from (10), as the BOMPD is required to generate a dc error signal that is used to lock the tunable oscillator onto the reference. Therefore, in (10), there should be a k such that $\omega_{\mathrm{RF}} = k\omega_{\mathrm{ref}}$. The BOMPD characteristic function, $H(\phi)$, consequently can be derived as the dc term in (10) multiplied by the photodiode responsivity

$$H(\phi) \approx \alpha I_{x,\mathrm{avg}} R \sin(\phi) \tag{12}$$

where R is the photodiode responsivity. By increasing the RF modulation amplitude, the modulator enters the nonlinear regime in which case the linear approximation of (10) has a high error. Finding the exact form of the BOMPD characteristic function using the Fourier series expansion of $I_x(t)$ and $\sin(\psi)$ is a tedious task. It is much easier to find the characteristic function of the BOMPD using direct integration and avoid the Fourier series expansion. Applying the condition of harmonic locking, $\omega_{\mathrm{RF}} = k\omega_{\mathrm{ref}}$, to (6) results in a periodic function with a period of T_{ref}. Averaging over one period of this function leads to the phase detector characteristic function

$$\begin{aligned} H(\phi) &= \frac{R}{T_{\mathrm{ref}}} \int_{<T_{\mathrm{ref}}>} \mathrm{d}t\, \Delta I_y(t) \\ &= \frac{R}{T_{\mathrm{ref}}} \int_0^{T_{\mathrm{ref}}} \mathrm{d}t\, I_{x,\mathrm{avg}} T_{\mathrm{ref}} \delta(t) \sin[\alpha \sin(\omega_{\mathrm{RF}} t + \phi) + \psi_{\mathrm{dc}}] \\ &= I_{x,\mathrm{avg}} R \sin[\alpha \sin(\phi) + \psi_{\mathrm{dc}}]. \end{aligned} \tag{13}$$

This result is identical to what is derived in [29], but our derivation is much more compact and also the dependence of the BOMPD characteristic function on the bias point variation is considered. Depending on the value of ψ_{dc}, this characteristic function will have different properties that are discussed in Section II-B.

B. Theory of OEPLL Using BOMPD

In this section, the necessary conditions of phase locking of OEPLL shown in Fig. 2(a) using BOMPD are discussed. The characteristic functions of the BOMPD are shown in Figs. 4 and 5 for different conditions. The slope of these curves at their operating point will be the phase detector gain. Using an RC loop filter to integrate the output current of the BOMPD (similar to type-II charge pump PLLs) forces the steady-state current to be zero [30]. This makes the BOMPD operating point (ϕ) and gain independent of the required tuning voltage for tunable oscillator. Therefore, the BOMPD requires at least one zero crossing in its characteristic function curve. From this point, when we refer to phase detector gain, we mean the phase detector gain at the zero crossing.

The characteristic function in (13) scales with $I_{x,\mathrm{avg}} R$ and its shape varies with respect to two variables, α and ψ_{dc}. An important scenario is when the modulator is biased at the odd symmetry point and $H(\phi)$ becomes

$$H(\phi) = I_{x,\mathrm{avg}} R \sin[\alpha \sin(\phi)]. \tag{14}$$

Therefore, $H(\phi)$ has an odd symmetry and the characteristic function has a zero at $\phi = 0$. Another feature of $H(\phi)$ can be derived from (13)

$$H\left(\pm\frac{\pi}{2} + \phi\right) = H\left(\pm\frac{\pi}{2} - \phi\right). \tag{15}$$

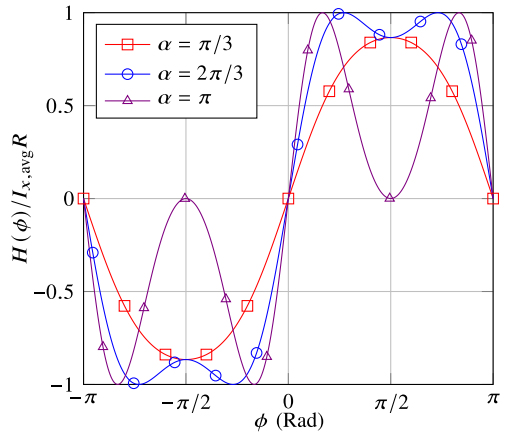

Fig. 4. Phase detector characteristic curve for different RF excitation amplitudes.

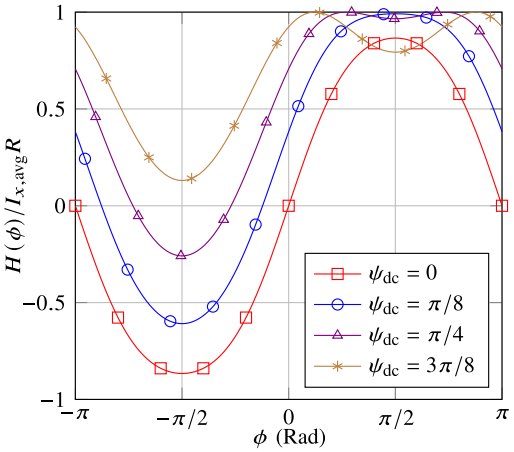

Fig. 5. Phase detector characteristic curve for different bias points.

In other words, the characteristic function has an even symmetry around $\phi = \pm\pi/2$. Therefore, the zeros of the characteristic function come in pairs that are symmetric around $\phi = \pm\pi/2$. These pairs correspond to phase detection gains with equal amplitudes and opposite signs, which can be seen in Figs. 4 and 5 as the slope of the characteristic function around the zero crossings. Depending on the slope of the VCO tuning characteristic, the OEPLL locks either with the positive or the negative gain of BOMPD.

Another effect that can be seen in Fig. 4 is that as the RF modulation amplitude increases, more zeros may appear in the characteristic function. However, these zeros correspond to relatively high modulation amplitudes. Increasing the RF amplitude to $V_{\pi,\mathrm{RF}}$ (which corresponds to $\alpha = 1$) leads to two additional zeros at $\phi = \pm\pi/2$. The phase detector gain at these zeros is zero or practically very low, and therefore, the loop cannot lock on these points. In addition, considering currently available $LiNbO_3$ modulators with V_π of approximately 4 V, an RF excitation of V_π corresponds to medium-range RF power levels in the 50-Ω system, which are suitable for low-noise and wideband applications. We, therefore, avoid further discussion of additional zeros in the transfer characteristics and limit our discussion to RF excitation voltages below V_π.

Fig. 5 shows the effect of the modulator's bias point variation on the BOMPD characteristic function. It can be seen that as the bias point moves toward the $\psi = \pi/2$ even symmetry point, the zero-crossing point moves toward negative values of ϕ and the function is shifted upward and its shape also changes. One of the zero crossings of $H(\phi)$ can be found using (13) as

$$\phi_0 = -\arcsin\left(\frac{\psi_{\mathrm{dc}}}{\alpha}\right) \quad \text{where} \quad |\psi_{\mathrm{dc}}| \le \alpha. \tag{16}$$

The other zero of $H(\phi)$ can be found using (15). If the absolute value of the offset phase exceeds α, then the transfer characteristic will not have any zeros, and therefore, the OEPLL will not lock. One can see in Fig. 5 that as the phase offset ψ_{dc} increases, the slope of $H(\phi)$ at its zero crossing decreases. Also, since the phase detector follows the relation in (15), its gain has the same absolute value for both zero crossings with opposite signs. It is usually desired to maximize the phase detector gain, as it minimizes the in-band noise of the other components. However, changing the bias point can be used as a degree of freedom to change the phase detector gain and, consequently, the loop bandwidth. The phase detector gain can be found as the derivative of $H(\phi)$ using (13) and (16)

$$\begin{aligned} K_\phi &= \alpha I_{x,\mathrm{avg}} R \cos(\phi_0)\cos[\alpha\sin(\phi_0) + \psi_{\mathrm{dc}}] \\ &= I_{x,\mathrm{avg}} R\sqrt{\alpha^2 - \psi_{\mathrm{dc}}^2}. \end{aligned} \tag{17}$$

From (17), it can be seen that K_ϕ is affected by quite a few parameters, such as MLL power, photodetector responsivity, VCO amplitude, MZM parameters, and MZM dc bias. Equations (1), (2), and (17) are used to calculate the transfer function of the OEPLL and provide a basic mathematical model of the OEPLL.

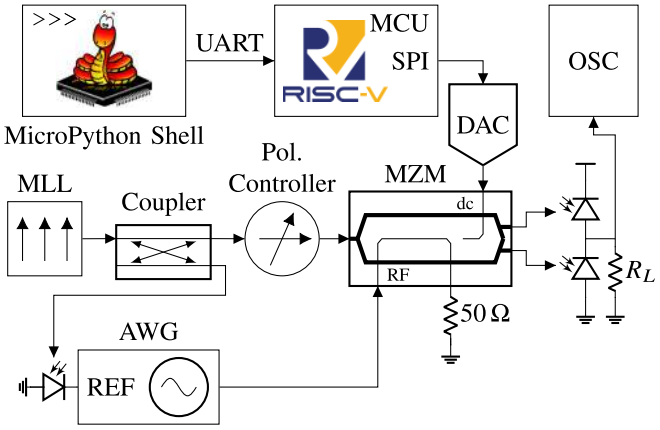

Fig. 6. Test setup for characterization of BOMPD. MCU: microcontroller unit. DAC: digital-to-analog converter. MLL: mode-locked laser. MZM: Mach–Zehnder modulator. Pol. Controller: polarization controller. AWG: arbitrary waveform generator. OSC: oscilloscope.

III. Measurement Results

A. Characterization of BOMPD

The BOMPD has been characterized using the block diagram shown in Fig. 6. The optical frequency reference from the MLL is divided into two parts: a strong coupling goes to the MZM and weak coupling is used as a frequency reference to

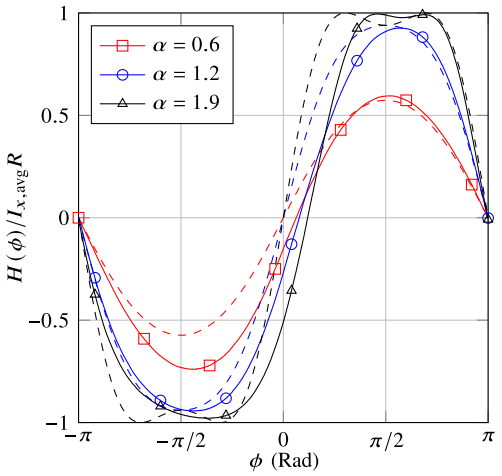

Fig. 7. Measured (solid line) and theoretical (dashed line) phase detector characteristic curves at the odd symmetry point for different RF amplitudes: (red) $\alpha = 0.6$, (blue) $\alpha = 1.2$, and (black) $\alpha = 1.9$.

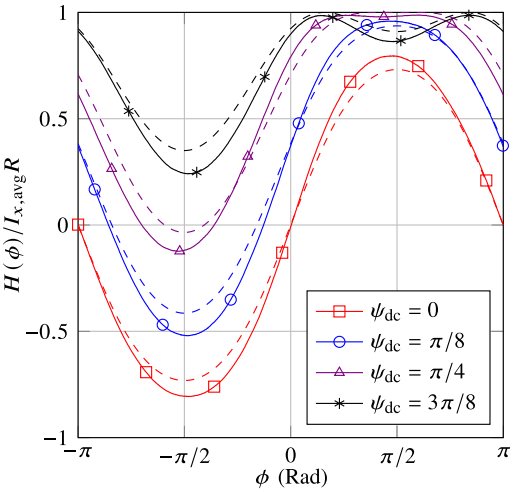

Fig. 8. Measured (solid line) and theoretical (dashed line) phase detector characteristic curves at $\alpha = 0.8$ for different bias points: (red) $\psi_{dc} = 0$, (blue) $\psi_{dc} = \pi/8$, (violet) $\psi_{dc} = \pi/4$, and (black) $\psi_{dc} = 3\pi/8$.

synchronize the arbitrary waveform generator (AWG) with the optical reference. The BOMPD output current is converted into a voltage via a load resistor, R_L. This voltage is then monitored with an oscilloscope. The MZM bias point is set via a DAC, which is controlled via an RISC-V microcontroller uploaded with a MicroPython firmware. The MZM bias control is performed in an open-loop fashion. The required bias voltages for the desired operating points are measured separately and stored in a lookup table inside the microcontroller.

The proposed setup can discriminate the phase difference between the harmonics of the optical reference and the output voltage according to (13). By introducing an offset frequency with respect to the n'th harmonic of the reference, the phase can be continuously swept

$$f_{\mathrm{AWG}} = n f_{\mathrm{ref}} + \Delta f \tag{18}$$

where f_{AWG} is the frequency of the AWG instrument and Δf is the offset frequency. The relation between the phase difference ϕ in (13) and the offset frequency Δf in (18) then simply is

$$\phi = 2\pi\, \Delta f t. \tag{19}$$

Figs. 7 and 8 compare the measurement results with the characteristic function derived in (13) for different RF amplitudes and different MZM bias points, respectively. In deriving the BOMPD characteristic function, it was assumed that the MZM is loss-less, and therefore, the intensity $I_{x,\mathrm{avg}}$ in (13) was determined with reference to the output of the MZM. The results show a good matching between the theory developed in this article and the measured results. The difference between the theory and practice in these plots can be attributed to nonidealities that were ignored in deriving (4) such as optical and electrical velocity mismatch in the modulator, nonlinearity and asymmetry in the pair of photodiodes, and the harmonic content of the RF modulation signal. The MLL pulsewidth is sub-200 fs, which corresponds to bandwidths of hundreds of gigahertz. Therefore, the approximation of the optical pulse shape with the Dirac delta function in (8) is highly accurate and the optical pulsewidth does not play a major role in the discrepancy between the measured and the theoretical plots in Fig. 7.

B. OEPLL Setup and Characterization

Fig. 9 shows the block diagram of the implemented OEPLL. The core of this setup is similar to the block diagram shown in Fig. 2(a). An yttrium iron garnet (YIG) oscillator with a bandwidth of 2–20 GHz is used as a tunable oscillator because of its high bandwidth and low phase noise. The main coil of the YIG oscillator has a high tuning sensitivity and is used to coarse-tune the frequency. The current of this coil is set via a current driver circuit and a low-noise DAC. The FM coil is driven with a low-noise operational amplifier (Op-Amp), which gets its input voltage from the loop filter output voltage. The optical reference is an MLL from Menhir photonics with a center wavelength of 1560 nm, a repetition rate of 250 MHz, and a pulsewidth below 200 fs [12]. The BOMPD was implemented with a lithium niobate ($LiNbO_3$) MZM with complementary outputs and a pair of InGaAs photodiodes to convert the optical output of the MZM into an electrical current. The output current pulses of the photodiode pair are then integrated via a series RC loop filter and converted into a voltage [30]. Since the MZM performance is sensitive to the polarization of the input optical field, a polarization controller is placed between the MLL and the MZM to align the polarization of the input field with the required polarization of the MZM. Another low-noise DAC controls the bias voltage of the dc electrode of the MZM.

The low-noise DACs are programmed via SPI interface. The SPI commands are sent from an RISC-V open-source instruction set microcontroller. The microcontroller is loaded with MicroPython firmware and receives Python commands from a computer.

The optical input power of the MZM was set to achieve a total average power of 1 mW at the outputs of the MZM. The MZM π-voltage for the RF electrode is approximately 4.5 V. The RF modulation power is 18 dBm (an average value for the whole band), which corresponds to an amplitude of 2.5 V in the 50-Ω system. Therefore, the numerical value for α is calculated from (11) as 1.75 rad. With a responsivity of 0.95 A/W for the photodiodes, according to (17), the BOMPD gain at the odd point of symmetry is 1.66 A/rad.

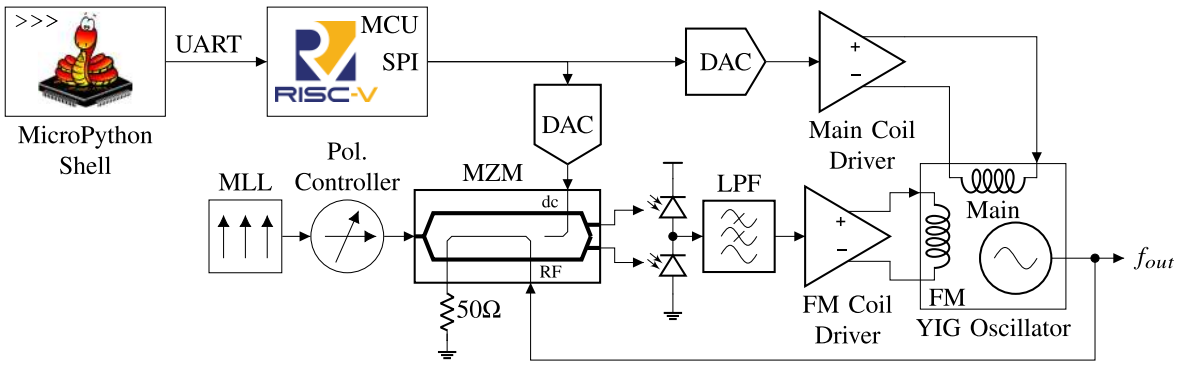

Fig. 9. Optoelectronic PLL using electro-optical phase detector. MCU: microcontroller unit. DAC: digital-to-analog converter. MLL: mode-locked laser. MZM: Mach–Zehnder modulator. Pol. Controller: polarization controller. LPF: low-pass filter. YIG: yttrium iron garnet.

The photodiode shot noise contribution to the single-sideband (SSB) phase noise of the BOMPD can be written as [1]

$$S_{\phi,\text{shot}} = \frac{2qRI_{x,\text{avg}}}{K_\phi^2} = \frac{2q}{I_{x,\text{avg}}R\alpha^2} \tag{20}$$

where q is the electron charge. The numerical value for the phase noise of the BOMPD can be found using (20) as 1.1×10^{-16} or approximately -160 dBc/Hz. The PLL loop filter components were designed for a target loop bandwidth using the procedure in the reference books for the charge pump PLLs [30]. The designed values were then optimized using the ac simulation engine of the Keysight Advanced Design System (ADS) tool to achieve the target loop bandwidth and phase margin. On the one hand, the in-band phase noise of the output signal is dominated by the sum of the phase noise of the frequency reference (MLL) and the phase detector (BOMPD) according to (2). On the other hand, the out-of-band phase noise is mainly determined by the phase noise of the tunable oscillator (YIG oscillator) according to (3). Therefore, a good choice of loop cutoff frequency would be at the intersection of these phase noise plots. However, the optimum loop bandwidth for minimum integrated rms-jitter could be lower than the loop bandwidth found using the procedure explained. This is mainly because the high-pass behavior of the output phase to the tunable oscillator phase transfer function is not ideal and has a transition band. The contribution of the phase noise of the BOMPD in this transition band can be significant since the jitter scales linearly with the frequency. As a result, shifting the loop bandwidth even by a few hundreds of kilohertz to higher frequencies would result in a significant increase of the integrated rms-jitter as the phase noise of the BOMPD is higher than the phase noise of the tunable oscillator in the transition band.

The sum of the phase noise of the MLL and the BOMPD was estimated with a wideband loop predesign. The BOMPD noise level was measured to be around -150 dBc/Hz. This value is 10 dB higher than what was calculated using (20). One reason for this difference is that the dynamic $V_{\pi,\text{RF}}$ of the modulator (with RF signal stimulation) could be higher than the given static value (measured with dc voltage stimulation) provided by the manufacturer. This consequently decreases the phase detector gain and increases the phase noise according to (20). In addition, the FM coil driver adds more noise inside the loop bandwidth, which contributes to the measured

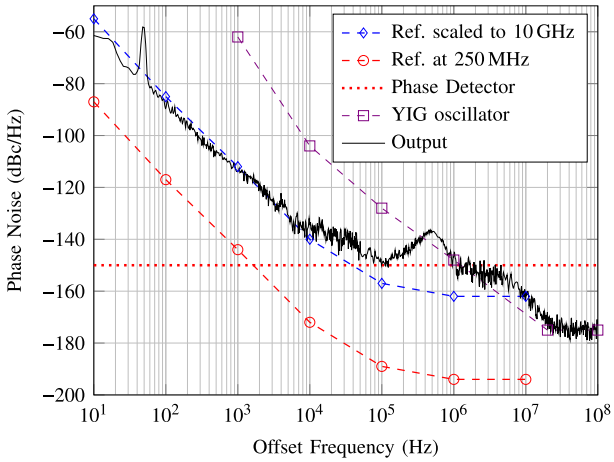

Fig. 10. Open-loop reference phase noise scaled to 10-GHz carrier frequency (blue dashed line), open-loop reference phase noise at the repetition rate 250 MHz (red dashed line), estimated phase noise of the phase detector (red dotted line), open-loop YIG oscillator phase noise (violet dashed line), and phase noise of the output signal of the OEPLL at 10-GHz carrier frequency (black line).

phase detector noise and causes the discrepancy between the measured phase noise of the phase detector and the numerical value calculated from (20). The YIG oscillator reaches the phase noise level of -150 dBc/Hz at 10-GHz carrier frequency at approximately 1-MHz offset frequency. Therefore, the loop was first designed for a 1-MHz loop bandwidth and later it was optimized for minimum integrated rms-jitter. The loop bandwidth can be fine-tuned by changing the bias point of the MZM, which consequently changes the phase detector gain.

Fig. 10 shows the phase noise of the output signal of the OEPLL at 10-GHz carrier frequency along with the open-loop phase noise of the reference, the phase detector, and the YIG oscillator. The phase noise data of the MLL and the YIG oscillator has been provided by the manufacturer. The loop bandwidth is approximately 500 kHz and the cutoff frequency of the closed-loop system can be seen as a bump in the phase noise plot of the output of the OEPLL. At very low offset frequencies below 10 kHz, the phase noise is dominated by the phase noise of the reference, and the phase detector does not have a significant contribution to the overall phase noise. In the intermediate offset frequency range inside the loop bandwidth, from 10 to 500 kHz, the output phase noise is mainly dominated by the phase noise of the phase detector. Outside

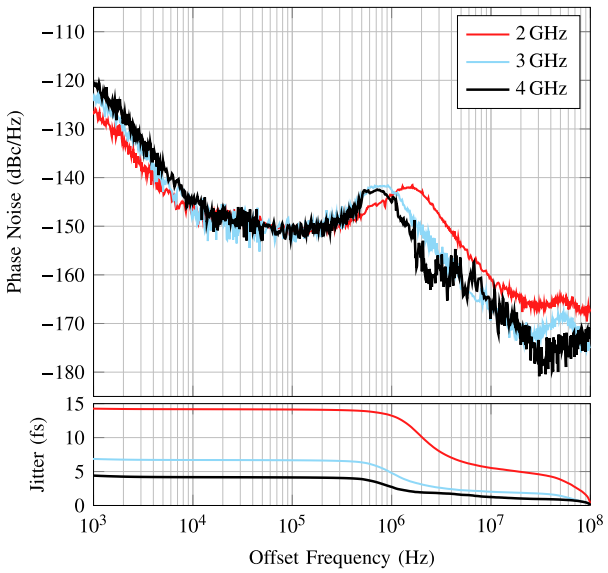

Fig. 11. Top: measured phase noise. Bottom: integrated rms-jitter at (red) 2-GHz, (cyan) 3-GHz, and (black) 4-GHz carrier frequencies.

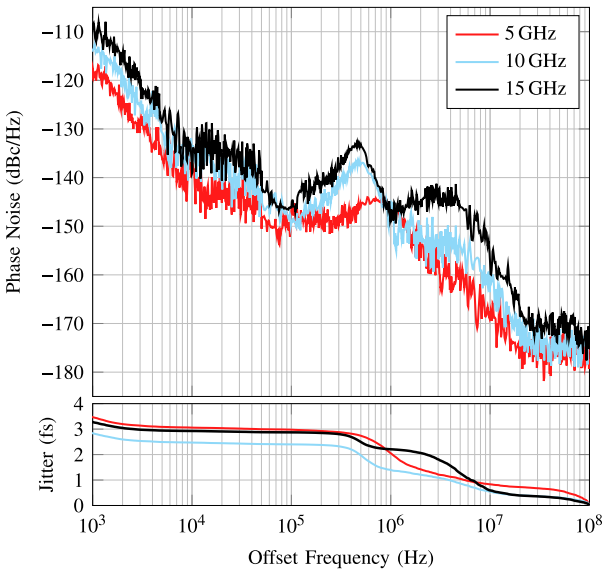

Fig. 12. Top: measured phase noise. Bottom: integrated rms-jitter at (red) 5-GHz, (cyan) 10-GHz, and (black) 15-GHz carrier frequencies.

the loop bandwidth at offset frequencies above 500 kHz, the output phase noise reaches the phase noise of the YIG oscillator. At frequencies close to the loop cutoff frequency, the output phase noise is mainly determined by the phase noise of the YIG oscillator and the phase detector. The bump at the cutoff frequency is due to higher phase noise of the YIG oscillator at the cutoff frequency.

The jitter and the phase noise are related via

$$\text{Jitter} = (\text{Phase Noise})/2\pi f_c \tag{21}$$

where f_c is the carrier frequency. The integrated rms-jitter can be calculated by integrating the jitter power spectral density. Figs. 11–13 show the measured phase noise and the integrated rms-jitter of the OEPLL output signal at different carrier frequencies in the frequency range of 2–20 GHz. The MZM bias point was changed to achieve the optimum bandwidth for minimum integrated rms-jitter. The loop cutoff frequency can be identified in Figs. 11–13 at the offset frequency where the phase noise plot reaches a local maximum. The minimum and maximum cutoff frequencies are 450 kHz and 1.5 MHz corresponding to 15- and 2-GHz carrier frequencies, respectively. The loop cutoff frequency marks the transition from the phase noise of the reference and the phase detector to the phase noise of the YIG oscillator. The YIG oscillator has a better open-loop phase noise performance in the middle and at the end of its frequency range compared to the beginning of the frequency range. Therefore, at the lower carrier frequencies, the phase detector phase noise plot coincides with the YIG phase noise plot at higher offset frequencies. This results in a higher optimum loop bandwidth for the frequencies at the beginning of the band.

The phase noise level of the BOMPD can be seen in Fig. 11 for the 2-GHz carrier frequency at the offset frequencies between 20 and 200 kHz, where the curve reaches a plateau. The loop bandwidth at this carrier frequency is approximately 1.5 MHz at the offset frequency where the phase noise plot has a local maximum. The main contributor to the phase noise

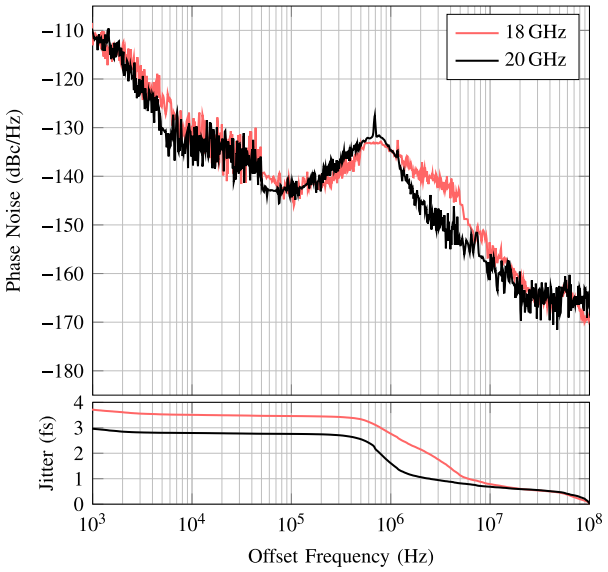

Fig. 13. Top: measured phase noise. Bottom: integrated rms-jitter at (red) 18-GHz and (black) 20-GHz carrier frequencies.

at this offset frequency is the phase noise of the YIG oscillator since the phase noise of the BOMPD is at −150 dBc/Hz and approximately 8 dB lower than the magnitude of this local maximum. The magnitude of this peak can be reduced by increasing the loop bandwidth to further suppress the YIG phase noise at lower offset frequencies. However, this increases the phase noise contribution of the BOMPD in the transition band (from the BOMPD phase noise to the YIG oscillator phase noise) and also the integrated rms-jitter. The same argument holds for the phase noise plots at other carrier frequencies. The rms-jitter integrated from 1 kHz to 100 MHz is also shown in Figs. 11–13. The OEPLL has an integrated rms-jitter (1 kHz–100 MHz) of 15 fs at 2 GHz, 2.8 fs at 10 GHz, and 3 fs at 20 GHz. The maximum rms-jitter in the frequency range of 5–20 GHz is only 4 fs. The main

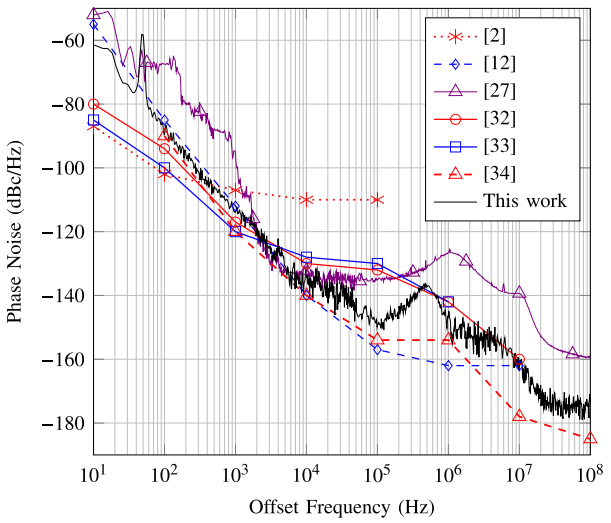

Fig. 14. Phase noise comparison of microwave frequency synthesizers at 10 GHz and frequency references normalized to 10-GHz carrier frequency: (red dotted line) 10-MHz quartz oscillator, (blue dashed line) Menhir MLL, (violet solid line) an octave-band OEPLL, (red solid line) Keysight E8257D, (blue solid line) R&S SMW200A, (red dashed line) single-frequency OEPLL, and (black solid line) this work.

reason for the higher jitter at the lower frequency range is that the YIG oscillator phase noise is approximately constant at all carrier frequencies and does not scale with it. Therefore, according to (21), a similar phase noise performance of an oscillator at different frequencies means higher jitter at lower frequencies. The YIG oscillator has higher phase noise at the beginning of the frequency range. This can be seen in the phase noise plot in Fig. 11 for the 2-GHz carrier frequency at offset frequencies above a few megahertz. These offset frequencies are outside the loop bandwidth, and the main contributor to the phase noise of the output signal is the phase noise of the YIG oscillator.

Fig. 14 compares the phase noise of the OEPLL with the state-of-the-art laboratory signal generators as well as OEPLLs. Compared to the wideband laboratory signal generators [32], [33], the OEPLL shows superior phase noise performance at offset frequencies above 2 kHz, especially in the intermediate frequency range below 500 kHz, which lies inside the loop bandwidth. The phase noise performance of the OEPLL and the state-of-the-art frequency synthesizers is similar at the offset frequencies above approximately 1 MHz, which is outside the loop bandwidth (at 10-GHz carrier frequency). This can be attributed to similar tunable oscillator technology for both the state of the art and the OEPLL. At offset frequencies below 2 kHz, the phase noise of the state-of-the-art instruments follows the quartz oscillator phase noise, which is better than that of the MLLs and consequently better than that of the OEPLL. This poor performance at lower frequencies below 2 kHz can indeed be improved by locking the MLL on a quartz reference.

Compared to our previous OEPLL reported in [27], this work has better phase noise at almost all offset frequencies. The main reason for this improvement is using a YIG oscillator instead of an integrated VCO, as YIG oscillators have resonators with higher quality factors and consequently better phase noise. The phase noise performance of the OEPLL reported in [34] is similar to this work at offset frequencies below 10 kHz. However, [34] has lower phase noise at offset frequencies above 10 kHz. The superior performance of [34] at higher offset frequencies is mainly due to the lower open-loop phase noise of the DRO used as the tunable oscillator. The additive phase noise of [34] has been reported in [25] and can be compared with that of our OEPLL. The additive phase noise of this work can be considered as the difference between the reference phase noise and the output signal phase noise. Since the phase noise of the tunable oscillator is suppressed inside the loop bandwidth, the main source of the additive phase noise is the phase detector noise. This explains the approximately flat shape of the additive phase noise in [25], as the source of the phase detector noise is the shot noise of the photodiodes. Although the additive phase noise of this work was not measured, its in-band level can be estimated to be the phase detector noise (approximately −150 dBc/Hz). The phase detector noise can be observed at lower carrier frequencies (see Fig. 11), where the reference phase noise is well below the phase detector noise. The phase detector noise shows itself as a plateau in the frequency range between 20 and 200 kHz. Therefore, the inside-loop additive phase noise of this work is 4 dB higher than that of the OEPLL reported in [25], which is −154 dBc/Hz normalized to 10-GHz carrier frequency.

The phase noise of our OEPLL can be compared with other RF signal generation methods such as SLCO and direct detection of the optical pulse whose phase noise plots are shown in Fig. 1. The SLCOs reported in [5] and [6] perform better than this work because of superior performance of SLCO compared to our MLL and also the phase noise of the BOMPD inside the loop bandwidth. The additive noise of the direct detection scheme is usually limited by the difference of the RF power to the thermal noise floor, which can be improved by increasing the RF power using the pulse interleaving technique and high-power photodiodes. Therefore, a combination of the best in class MLL and a direct detection receiver have a better phase noise than that of this OEPLL by more than two orders of magnitude [6], [14]. Although these works have lower phase noise, they have a single-frequency output, whereas our OEPLL has an output frequency range from 2 to 20 GHz.

IV. Conclusion

This article presented a theory and application of a wideband low-jitter OEPLL. A nonlinear model of the transfer characteristic of BOMPD as phase detector is derived and applied to a linear model of the OEPLL, similar to classical PLL theory. The OEPLL can lock on any of the harmonics of the envelope of the optical pulse train of an MLL in the frequency range from 2 to 20 GHz. The electronic output signal of the OEPLL exhibits a typical in-band (10 kHz–1 MHz) phase noise below −140 dBc/Hz and a minimum of −150 dBc/Hz. The integrated rms-jitter (1 kHz–100 MHz) of the OEPLL is as low as 4 fs in the 5–20-GHz frequency range. This OEPLL outperforms the best laboratory grade frequency synthesizers at offset frequencies higher than 2 kHz [32], [33], [35]. To the author's knowledge, this is the best reported jitter performance for any wideband frequency synthesizer so far.

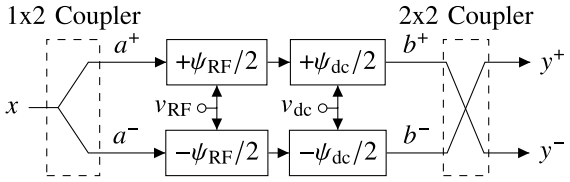

Fig. 15. Block diagram of MZM with two separate electrodes for RF modulation and dc bias.

APPENDIX
GOVERNING EQUATION OF BIM

As we mentioned earlier, the BIM can be implemented using a Sagnac loop or an MZM, as they both have similar transfer characteristics. We therefore choose a balanced MZM block diagram, shown in Fig. 15, for our analysis. Assuming that the photodetectors in Fig. 2(a) are linear, we can directly use the output intensities of the MZM and exclude the photodiode responsivity from our equations. The input optical field, x, is divided into two parts and these parts enter the upper and the lower arms of the modulator. Each part passes through two tunable phase shifters that are controlled by two separate electrodes, RF and dc. The upper and the lower phase shifters add positive and negative phase shifts to the optical signals, respectively. The phase-shifted signals are then recombined using a 90° 2×2 coupler, which obeys the following relations in the phasor domain:

$$y^+ = \frac{b^+ + jb^-}{\sqrt{2}} \quad \text{and} \quad y^- = \frac{b^- + jb^+}{\sqrt{2}} \tag{22}$$

where y^+ and y^- are the output signals of the coupler, b^+ and b^- are the input signals of the coupler, and j is the unit imaginary number $(-1)^{1/2}$.

The output signals of the 1×2 coupler, a^+ and a^-, are both equal to $x/(2)^{1/2}$. The outputs of the upper and lower phase shifters are then

$$b^{\pm} = \frac{x}{\sqrt{2}} e^{\pm j\psi/2} \tag{23}$$

where the phase ψ follows (5). Combining (22) and (23), the outputs of the modulator can be written as

$$y^{\pm} = \frac{x}{2}\left[e^{\pm j\psi/2} - je^{\mp j\psi/2}\right]. \tag{24}$$

The intensities of the optical outputs can consequently be derived as

$$I_y^{\pm} = I_x\left[0.5 \pm 0.5\sin(\psi)\right] \tag{25}$$

where I_y^+ is the intensity of y^+, I_y^- is the intensity of y^-, and I_x is the intensity of the optical input field x.

REFERENCES

[1] J. Kim and F. X. Kärtner, "Attosecond-precision ultrafast photonics," *Laser Photon. Rev.*, vol. 4, no. 3, pp. 432–456, Apr. 2010.

[2] *High Performance (VC)OCXO*, KVG Quartz Cryst. Technol. GmbH, Neckarbischofsheim, Germany, Datasheet O-40CXXXX-LPN-LGS-LF, Nov. 2017.

[3] *Ultra Low Phase Noise Oven Controlled Crystal Oscillator*, Vectron, Mount Holly Springs, PA, USA, Datasheet OX-305, Nov. 2016.

[4] *Voltage Controlled SAW Oscillator Surface Mount Model, Rev.B*, Synergy Microw., Paterson, NJ, USA, Datasheet HFSO1000-5, Mar. 2017.

[5] *The Sapphire Loaded Cavity Oscillator (SLCO)*, Poseidon Sci. Instrum., Fremantle WA, Australia, Datasheet SLCO, May 2004.

[6] J. W. Zobel *et al.*, "Comparison of optical frequency comb and sapphire loaded cavity microwave oscillators," *IEEE Photon. Technol. Lett.*, vol. 31, no. 16, pp. 1323–1326, Aug. 15, 2019.

[7] L. Maleki, "Optoelectronic oscillators for microwave and mm-wave generation," in *Proc. 18th Int. Radar Symp. (IRS)*, Jun. 2017, pp. 1–5.

[8] A. B. Matsko, D. Eliyahu, and L. Maleki, "Theory of coupled optoelectronic microwave oscillator II: Phase noise," *J. Opt. Soc. Amer. B, Opt. Phys.*, vol. 30, no. 12, p. 3316, Nov. 2013.

[9] A. Ly, V. Auroux, R. Khayatzadeh, N. Gutierrez, A. Fernandez, and O. Llopis, "Highly spectrally pure 90-GHz signal synthesis using a coupled optoelectronic oscillator," *IEEE Photon. Technol. Lett.*, vol. 30, no. 14, pp. 1313–1316, Jul. 15, 2018.

[10] T. K. Kim *et al.*, "Sub-100-as timing jitter optical pulse trains from mode-locked Er-fiber lasers," *Opt. Lett.*, vol. 36, no. 22, p. 4443, Nov. 2011.

[11] "Ultra low timing jitter performance & characterization of origami femtosecond laser series, rev. 1.1," Onefive, Berlin, Germany, White Paper P/N 09-001, Jun. 2009.

[12] *Menhir Photonics Femtosecond Laser Source*, Menhir Photonics AG, Rümlang, Switzerland, Datasheet MENHIR-1550, Jun. 2019.

[13] X. Xie *et al.*, "Photonic microwave signals with zeptosecond-level absolute timing noise," *Nature Photon.*, vol. 11, no. 1, pp. 44–47, Nov. 2016.

[14] M. Kalubovilage, M. Endo, and T. R. Schibli, "Ultra-low phase noise microwave generation with a free-running monolithic femtosecond laser," *Opt. Exp.*, vol. 28, no. 17, p. 25400, Aug. 2020.

[15] S. Krakauer, "Harmonic generation, rectification, and lifetime evaluation with the step recovery diode," *Proc. IRE*, vol. 50, no. 7, pp. 1665–1676, Jul. 1962.

[16] E. Afshari and A. Hajimiri, "Nonlinear transmission lines for pulse shaping in silicon," *IEEE J. Solid-State Circuits*, vol. 40, no. 3, pp. 744–752, Mar. 2005.

[17] T. D. Shoji *et al.*, "Ultra-low-noise monolithic mode-locked solid-state laser," *Optica*, vol. 3, no. 9, p. 995, Sep. 2016.

[18] J. Millo *et al.*, "Ultra-low-noise microwave extraction from fiber-based optical frequency comb," *Opt. Lett.*, vol. 34, no. 23, p. 3707, Nov. 2009.

[19] T. M. Fortier *et al.*, "Generation of ultrastable microwaves via optical frequency division," *Nature Photon.*, vol. 5, no. 7, pp. 425–429, Jun. 2011.

[20] F. Quinlan *et al.*, "Ultralow phase noise microwave generation with an Er: Fiber-based optical frequency divider," *Opt. Lett.*, vol. 36, no. 16, p. 3260, Aug. 2011.

[21] W. Zhang, S. Seidelin, A. Joshi, S. Datta, G. Santarelli, and Y. L. Coq, "Dual photo-detector system for low phase noise microwave generation with femtosecond lasers," *Opt. Lett.*, vol. 39, no. 5, p. 1204, Feb. 2014.

[22] J. Kim, F. X. Kärtner, and F. Ludwig, "Balanced optical-microwave phase detectors for optoelectronic phase-locked loops," *Opt. Lett.*, vol. 31, no. 24, p. 3659, Nov. 2006.

[23] M. Y. Peng, A. Kalaydzhyan, and F. X. Kärtner, "Balanced optical-microwave phase detector for sub-femtosecond optical-RF synchronization," *Opt. Exp.*, vol. 22, no. 22, p. 27102, Oct. 2014.

[24] J. Kim, F. X. Kärtner, and M. H. Perrott, "Femtosecond synchronization of radio frequency signals with optical pulse trains," *Opt. Lett.*, vol. 29, no. 17, p. 2076, Sep. 2004.

[25] K. Jung and J. Kim, "Subfemtosecond synchronization of microwave oscillators with mode-locked Er-fiber lasers," *Opt. Lett.*, vol. 37, no. 14, p. 2958, Jul. 2012.

[26] A. H. Nejadmalayeri and F. X. Kärtner, "Mach-Zehnder based balanced optical microwave phase detector," in *Proc. Conf. Lasers Electro-Opt.*, 2012, pp. 1–2.

[27] M. Bahmanian, J. Tiedau, C. Silberhorn, and J. C. Scheytt, "Octave-band microwave frequency synthesizer using mode-locked laser as a reference," in *Proc. Int. Topical Meeting Microw. Photon. (MWP)*, Oct. 2019, pp. 1–4.

[28] M. Bahmanian, S. Fard, B. Koppelmann, and J. C. Scheytt, "Ultra low phase noise and ultra wide-band frequency synthesizer using an optical clock source," in *IEEE MTT-S Int. Microw. Symp. Dig.*, Aug. 2020, pp. 1283–1286.

[29] T. Lamb, "Laser-to-RF phase detection with femtosecond precision for remote reference phase stabilization in particle accelerators," Ph.D. dissertation, Technische Universität Hamburg Harburg, Hamburg, Germany, 2017. [Online]. Available: http://bib-pubdb1.desy.de/record/320841

[30] B. Razavi, *RF Microelectronics*. London, U.K.: Pearson, 2011.

[31] P. R. Gray, P. J. Hurst, and S. H. Lewis, *Analysis and Design of Analog Integrated Circuits*. Hoboken, NJ, USA: Wiley, 2009.

[32] *Microwave Analog Signal Generator*, Keysight, Santa Rosa, CA, USA, Datasheet E8257D, Feb. 2016.
[33] *Vector Signal Generator, Version 11.00*, Rohde Schwarz, Munich, Germany, Datasheet SMW200A, Dec. 2019.
[34] K. Jung, J. Shin, and J. Kim, "Ultralow phase noise microwave generation from mode-locked Er-fiber lasers with subfemtosecond integrated timing jitter," *IEEE Photon. J.*, vol. 5, no. 3, Jun. 2013, Art. no. 5500906.
[35] *RF/Microwave Signal Generator, Rev.R*, Anritsu, Kanagawa, Japan, Datasheet MG3690C, 2016.

Meysam Bahmanian received the B.Sc. degree from Amirkabir University, Tehran, Iran, in 2007, and the M.Sc. degree from the University of Freiburg, Freiburg, Germany, in 2016. He is currently pursuing the Ph.D. degree at Paderborn University, Paderborn, Germany.

His research interests include RF and mm-wave IC design, silicon photonics, and optoelectronic systems.

J. Christoph Scheytt (Member, IEEE) received the Diploma (M.Sc.) and Ph.D. degrees (Highest Hons.) from Ruhr-University Bochum, Bochum, Germany, in 1996 and 2000, respectively.

In 2000, he co-founded advICo microelectronics GmbH, a German IC design house for RFIC and fiber-optic IC design. For six years, he served as a CEO at advICo. From 2006 to 2012, he was the Head of the IHP's Circuit Design Department, IHP Leibnizinstitute for High-Performance Microelectronics, Frankfurt (Oder), Germany. In 2012, he was appointed as a Full Professor for Circuit Design by the University of Paderborn, Paderborn, Germany, and a Research Group Leader at the Heinz-Nixdorf Institute, Paderborn. Since 2016, he has been serving as the Chairman of the Board of Directors of the Heinz Nixdorf Institute. Since 2018, he has been the Leader of the Priority Program "Ultrafast Electronic-Photonic Integrated Systems for Ultrafast Signal Processing" SPP 2111 of the Deutsche Forschungsgemeinschaft. He has authored or coauthored more than 180 refereed journal papers and conference contributions and holds 20 patents. His research interests focus on high-frequency and broadband IC design for communications and sensing, IC design with SiGe BiCMOS and CMOS technologies, and silicon photonics.